NEURAL NETWORKS PARADIGM FOR ROTATING FLOW OF JEFFREY FLUID WITH HEAT TRANSFER BETWEEN TWO PARALLEL HORIZONTAL PLATES

by

Ibrahim MAHARIQ [a,b,c,d], ***Saeed ISLAM*** [e*], ***Ishtiaq ALI*** [f], ***Mehreen FIZA*** [g], ***Ajed AKBAR*** [g], ***Syed Arshad ABAS*** [g], ***Hakeem ULLAH*** [g*], ***and Ali AKGUL*** [h,i,j,k*]

[a] Najjad Zeenni Faculty of Engineering, Al-Quds University, Jerusalem, Palestine
[b] University College, Korea University, Seoul, South Korea
[c] Department of Medical Research, China Medical University Hospital, China Medical University, Taichung, Taiwan
[d] Applied Science Research Center, Applied Science Private University, Amman, Jordan
[e] Department of Mechanical Engineering, Prince Mohammad Bin Fahd University, Al Khobar Saudi Arabia
[f] Department of Mathematics and Statitics, College of Science, King Faisal University, Al-Ahsa, Saudi Arabia
[g] Department of Mathematics, Abdul Wali Khan University, Mardan, Khyber Pakhtunkhwa, Pakistan
[h] Department of Electronics and Communication Engineering, Saveetha School of Engineering, SIMATS, Chennai, Tamilnadu, India
[i] Siirt University, Art and Science Faculty, Department of Mathematics, Siirt, Turkey
[j] Applied Science Research Center, Applied Science Private University, Amman, Jordan
[k] Department of Computer Engineering, Biruni University, Topkapı, Istanbul, Turkey

Original scientific paper
https://doi.org/10.2298/TSCI2505681M

The current research explores the analysis of heat transfer in the rotating Jeffrey fluid between two parallel plates, employing the BLMS-ANN approach based on the back propagation Levenberg-Marquardt scheme. The fluid-flow is initially described by a system of PDE, which is subsequently transformed into a system of ODE through appropriate correspondence transformations and boundary conditions. Eventually, the equations are rendered dimensionless using a boundary-layer approximation. By changing parameters including the radiation parameter, Rd, Deborah number, λ, viscosity parameter, R, Prandtl number, Reynolds number, and Rotation parameter, kr, using the differential transform method, a group of data for suggested BLMS-ANN is constructed for several cases. To assess the predicted outcomes for specific scenarios, the BLMS-ANN methodology undergoes testing validation and training. Subsequently, the proposed model is scrutinized for confirmation. The validity of the suggested BLMS-ANN approach is confirmed through regression analysis, examination of mean square error, and histogram studies. The suggested method differs from both the proposed and reference results with an accuracy level between.

Key words: *Jeffrey nanofluid, rotating system, differential transform method, neural networks Levenberg-Marquardt method, steady flow*

* Corresponding authors, e-mail: sislam@pmu.edu.sa; hakeemullah1@gmail.com; aliakgul00727@gmail.com

Introduction

The ANN are intriguing and important frameworks connected with artificial intelligence (AI). Depending on input which passes through network during the learning process, whether external or internal, ANN can take on a number of structures. The ANN employs back propagation (BP) approach to implement immediate working out to improve the performance of a multi-layer perceptron network. This is most widely applied, successful, and simple to learn model for complicated multi-layered systems. Scheme of Levenberg-Marquardt (LM) is a revolutionary, convergent, and efficient strategy for ANN that gives numerical solutions for various problems of fluid-flow. In 1973 the BP was used by Dreyfus, to change control system configurations in accordance to error gradients. Multi-layer network training was achieved by Werbos' (1975) BP method. He developed Linnainmaa's AD technique more well-known by using it with neural networks in 1982 [1, 2]. A common learning process in feed-forward multi-layer neural networks is BP.

This method recently employed by some examiners to scrutinize the flow of non-Newtonian fluids systems as well as elements of heat and heat transference. Using intelligent computing techniques, Ahmad *et al*. [3] examined the models of non-linear reactive fluid transport in micro-vessels and soft-tissues. Using neural networks, Shoaib *et al*. [4] examined creation of entropy in existence of heat radiation and MHD. Wang *et al*. [5] studied impact of wire array electrical characteristics on z-pinch load current. Uddin *et al*. [6] solved the mathematical simulation of unstable flow of thin film of magnetized Maxwell fluid on a horizontal revolving disk with chemical reaction and thermos diffusion impacts, using neural networks with back propagated by LM scheme NN-BLMS. In order to investigate the impact that magnetic fields and Hall current have on the micropolar flow of nanofluid between two rotating parallel plates, Ullah *et al*. [7] and Aljohani *et al*. [8] utilised ANN by employing a BP technique, because of the variations between non-Newtonian and Newtonian fluids, numerous non-Newtonian fluid models are developed. Fluids which are not following the Newtonian law of viscosity are referred to as non-Newtonian fluids. Ketchup, drilling muds, colloidal, certain oils, apple sauce, and suspension solutions are a few types of non-Newtonian fluids. A non-Newtonian fluid that has a temporal derivative rather than a convected derivative is a Jeffrey fluid, which is the most prevalent and basic model of these fluids. Zokri *et al*. [9] studied Jeffrey nanofluid-flow and MHD with viscous dissipation. Hayat *et al*. [10] explored the 3-D flow of Jeffrey fluid across a linearly stretched surface and used a homotopy analysis method to solve the non-linear coupled system of governing equations. Turkyilmazoglu and Pop [11] examined how a Jeffrey fluid moved and transferred heat across a shrinking/stretching sheet with a parallel outside flow close to the stagnation point. Shafique *et al*. [12] deliberated the rotating Jeffrey flow for binaries chemical reaction outcomes and activation energy. In the presence of nanoparticles, Nadeem *et al*. [13] investigated the continuous 2-D Jeffrey fluid-flow across a linearly stretched sheet. Das [14] explored the impacts of heat transfer and slip of flow of peristaltic Jeffrey fluid. Reddy *et al*. [15] study the flow of Jeffrey fluid between rotationally oscillating disks. Shehzad *et al*. [16] investigated non-linear thermal radiation of Jeffrey nanofluid in 3-D. Further relevant studies involving Jeffrey fluid can be found in the investigations [17-22] and numerous studies therein.

A significant number of articles have recently concentrated on employing nanofluid to improve the heat transfer process. Metal oxides and metal particles with maximum diameters of 100 nm suspended in ordinary fluids with low thermal conductivity, such as ethylene glycol, oil, pure water and so on, is known as nanofluid. The nanofluids have thermophysical properties that improve their performance. The heat transfer equipment shrinks in size due to

the use of nanofluids. To prevent aerodynamic friction, nanofluid are employed as a coolant in aero-dynamic design, resulting in considerable energy savings. Nanofluids are also utilized to accelerate heat transmission in transformers, biomedicine, fuel cells, heat exchangers, micropumps, computer microchips, and food processing systems [23-25]. Choi and Eastman [26] pioneered the use of nanofluids to increase thermophysical properties. Furthermore, he revealed experimentally that nanometer size particles are useful for raising the heat conductivity of the nanoparticles. Boungiorno [27] investigated the behavior of nanofluids in conservation equations by introducing the impacts of thermophoresis and Brownian diffusion. Kuznetsov and Nield [28] investigated the nanofluid-flow naturally convection of across a flat plate while accounting for double diffusion. Using a stretched sheet and a heat source/sink, Goyal and Bhargava [29] investigated the impact of velocity slip on the flow and heat transmission of a non-Newtonian nanofluid. Turkyilmazoglu [30] investigated a linear stability theory-based hydrodynamic stability study of various well-known nanofluids while taking into account of nanofluid model of single-phase. Ahmed *et al*. [31] studied various heat transport features of various nanofluids in a corrugated panel. They determined that Fe_3O_4-water nanofluid had a higher capacity for increasing thermal conductivity.

The fluids flow caused by a disk rotation problem is significant in industrial and technical purposes such as electronic devices, petroleum sector, computer storage devices, medical equipment, rotating machinery, MHD rotators, and so on. In 1921, the mathematician Von Karman [32] examine the fluid-flow issue in a revolving disc. This one is the most frequent problem with fluid dynamics. Greenspan [33] investigated the same phenomenon in a rotating system, whereas Vajravelua and Kumar [34] investigated hydro magnetic viscous fluid-flow in horizontal plates. Turkyilmazoglu [35] examined the influence of magnetic fields on laminar flow induced by rotating disc extension. In the analysis, he also addressed the heat transfer impact. Turkyilmazoglu [36] observed that the movement of working fluid caused by disk stretching is significant in cooling procedure of wall. Asghar *et al*. [37] employed the analysis of Lie group to examine the fluid-flow thermal analysis across a stretchy disk. Rashidi *et al*. [38] investigated the stretched spinning disk problem while generating entropy. Hayat *et al*. [39] investigated the slip process in the presence of MHD using a variable thickness spinning disk. Bachok *et al.* [40] demonstrated heat transmission and nanofluid boundary-layer flow through a spinning disc immersed in permeable media. Hayat *et al*. [41] utilized the HAM to examined the impact of a revolving disc on radiative flow.

While obtaining an accurate analytical solution of the problem can pose challenges, the scientist adopts a blend of numerical and semi-numerical approaches. These include methods such as HAM [42], spectral relaxation method [43], Galerkin finite element method [44], and Keller box technique [45]. The preceding investigation into nanofluid-flow across different fluidic systems employs a diverse range of semi-numerical and numerical techniques. Additionally, due to their effectiveness and efficiency, numerical computing intelligent systems are essential for implementing the RJF-HAP model. Machine learning techniques have also been integrated into stochastic numerical computing solutions, leveraging neural networks to address solutions for both linear and non-linear equations, showcasing diverse capabilities across various environments. When these procedures are combined, non-linear systems are created in various fields such as COVID-19 models [46, 47], and many other models flow models [48-52], and non-linear systems of equations [53-58] All of the mentioned literature drove the authors to study the topic and use stochastic approaches to create a new, better, more accurate computer model for fluid dynamics analysis, such the RJF-HAP model.

The following aspects provide perspectives on the suggested design-computing approach:

- The novel AI-based computational intelligence method known as the (RJF-HAP) model has been studied using ANN.
- The mathematical modelling of the ground-breaking scheme RJF-HAP in the form of PDE which has been converted to systems of ODE by making necessary relevant change.
- The DTM can be utilized to provide a dataset for the recommended BLMS-ANN as an alternate (RJF-HAP) to employing the radiation parameter, Deborah and Prandtl numbers, viscosity parameter, and rotation parameter.
- Modelling RJF-HAP for various scenarios employs BLMS-ANN training, validation, and testing methodologies, and assessment with alignment results validates the correctness of proposed BLMS-ANN.
- The mean square error (MSE), estimated fitness convergence graphs, regression metrics, and error histograms demonstrated the efficiency of the proposed BLMS-ANN in representing the RJF-HAP.

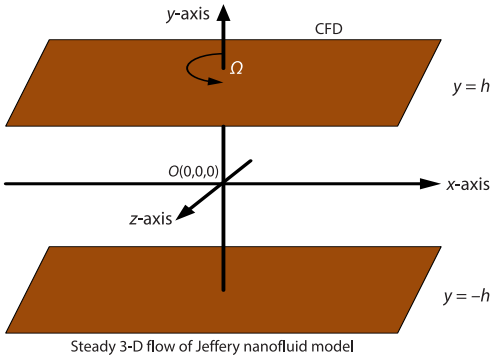

Figure 1. Flow problem geometry

Mathematical frame work of the model

The non-Newtonian Jeffrey fluid-flow is taken into account between two parallel, horizontal plates. Where is the distance between the lower and upper plates. The co-ordinate system that causes fluid and plate to revolve with an angular velocity of Ω around the *y*-axis. Stretch the lower plate along the *x*-axis to keep the origin constant, assuming that the two forces have the same magnitude but different directions. The fluid-flow is assumed to be in a steady-state where both mass and heat are transferred. The geometrical representation of the problem RJF-HAP is presented in fig. 1. From the previous consideration, the basic continuity equations, velocity, and energy are expressed and same as in [19, 20, 33, 34]:

$$\nabla V + 0$$

$$\rho \frac{\mathrm{d}V}{\mathrm{d}t} + 2\Omega \times V + \Omega \times (\Omega \times r) = \nabla V$$

The A_1 indicated first Rivilin-Erickson tensor, in component form:

$$\frac{\partial}{\partial x}(\overline{u}) + \frac{\partial}{\partial y}(\overline{v}) = 0 \tag{1}$$

$$\frac{\partial \overline{u}}{\partial x}(\overline{u}) - 2\overline{v}\Omega + \frac{\partial \overline{u}}{\partial y}(\overline{v}) = \frac{\mu}{\rho}\left(\frac{\partial}{\partial x}S_{xx} + \frac{\partial}{\partial y}S_{xy}\right) - \frac{1}{\rho}\frac{\partial p^*}{\partial x} \tag{2}$$

$$\frac{\partial \overline{v}}{\partial x}(\overline{u}) + 2\overline{u}\Omega + \frac{\partial \overline{v}}{\partial y}(\overline{v}) = \frac{\mu}{\rho}\left(\frac{\partial}{\partial x}S_{xy} + \frac{\partial}{\partial y}S_{yy}\right) - \frac{1}{\rho}\frac{\partial p^*}{\partial x} \tag{3}$$

$$\overline{u}\frac{\partial \overline{w}}{\partial x} + \overline{v}\frac{\partial \overline{w}}{\partial y} - (2\Omega)\overline{u} = \frac{\mu}{\rho}\left(\frac{\partial}{\partial x}S_{zx} + \frac{\partial}{\partial y}S_{zy}\right) \tag{4}$$

$$\frac{\partial T}{\partial x}\overline{u}+\frac{\partial T}{\partial y}\overline{v}=\frac{k}{\rho c_{p^*}}\frac{\partial^2 T}{\partial y^2}+\frac{\mu_0}{\rho c_{p^*}}S_{xy} \tag{5}$$

where $\overline{u}$, $\overline{v}$, and $\overline{w}$ are the velocity components, p^* – the modified pressure of fluid denoted the coefficient of kinematic viscosity, and ρ – the fluid density. In eq. (5), c_{p^*} is the specific heat, T – the temperature, k – the thermal conductivity, and μ_0 – the dynamic viscosity. Where S_{xx}, S_{xy}, and S_{yy} represent stress tensor components and Ω is the angular velocity. The physical behavior of flow phenomenon is presented

For Jeffrey fluid, Cauchy stress tensors are defined in [17-22]:

$$\Gamma=-\mathrm{P}I+S \tag{6}$$

$$S=\frac{\mu}{1+\lambda_1}\left(A_1+\lambda_2\frac{DA_1}{Dt}\right) \tag{7}$$

where I is the identity tensor and μ – the dynamic viscosity and ratio between relaxation and retardation time is represented with λ_1 and λ_2. The Revilan-Ericson tensor A_1 is expressed as $A_1 = (\nabla V)^T + (\nabla V)$ where V = [$\overline{u}$, $\overline{v}$, 0]. The S_{xx}, S_{xy}, and S_{yy} are the stress tensor components, determined and expressed:

$$S_{xx}=\frac{2\mu}{1+\lambda_1}\left[\frac{\partial\mu}{\partial x}+\lambda_2\left(\mu\frac{\partial^2\mu}{\partial x^2}+\overline{v}\frac{\partial^2\mu}{\partial y\partial x}\right)\right] \tag{8}$$

$$S_{xy}=\frac{\mu}{1+\lambda_1}\left[\frac{\partial\overline{u}}{\partial y}+\frac{\partial\overline{v}}{\partial x}+\lambda_2\left(\overline{u}\frac{\partial^2\overline{u}}{\partial y\partial x}+\overline{v}\frac{\partial^2\overline{u}}{\partial y^2}\right)\right]=S_{yx} \tag{9}$$

$$S_{yy}=\frac{2\mu}{1+\lambda_1}\left[\frac{\partial\overline{v}}{\partial y}+\lambda_2\left(\overline{u}\frac{\partial^2\overline{v}}{\partial y\partial x}+\overline{v}\frac{\partial^2\overline{v}}{\partial y^2}\right)\right] \tag{10}$$

The appropriate boundary conditions:

$$T=T_h,\ \overline{w}=0,\ \overline{v}=0,\ \overline{u}=ax,\ \text{at}\ y=0,\ \text{and}\ \overline{u}=0,\ \overline{w}=0,\ \overline{v}=0,\ T=T_0\ \text{at}\ y=h \tag{11}$$

Used non-dimensional variable:

$$\eta=\frac{y}{h},\ \overline{\mathrm{v}}=-ahF(\eta),\ \overline{u}=axF'(\eta),\ \overline{w}=ax\mathrm{g}(\eta),\ \Theta(\eta)=\frac{T-T_h}{T_0-T_h}\ \text{where}\ \eta=\frac{y}{h} \tag{12}$$

where $F'(\eta)$ is the derivative of F with respect to η. Using eqs. (6)-(10) in eqs. (1)-(5) are converted into to the form:

$$F^{iv}+(1+\lambda)\left(R\left(F'''F-F''F'\right)-2krG'\right)+\beta\left(2F''F'''-FF^{iv}-F'F^{v}\right)=0 \tag{13}$$

$$G''+(1+\lambda)\left(2krF'+R(FG'-GF')\right)+\beta(G'F''-FG''')=0 \tag{14}$$

$$\left(1+\frac{4}{3}Rd\right)\Theta''+\mathrm{Pr}\,\mathrm{Re}\,\Theta'=0 \tag{15}$$

$$F'(0)=1,\ G(0)=0,\ F(0)=0,\ \Theta(0)=1\ \text{at}\ \eta=0 \tag{16}$$

$$F'(1)=0,\ G(1)=0,\ F(1)=0,\ \Theta(1)=0 \tag{17}$$

After simplification, the physical parameters are obtained and defined as the Prandtl number $\mathrm{Pr} = \rho\nu c_{p^*}/k = \mu c_{p^*}/k$, the rotation parameter $kr = \Omega h/ax$, the radiation parameter $Rd = aT_c^4\varphi/kK$, the viscosity parameter $R = ah^2/\nu$ and $\lambda = \lambda_2 a$, and $\beta = \lambda_2\alpha$ is Deborah number.

Result and discussion

Figure 2 displays the proposed BLMS-ANN within the context of a neural network. The suggested BLMS-ANN were implemented using the *nftool*, a feature configuration method in the MATLAB neural network package. The weights of the networks were found using Levenberg-Marquardt back propagation. Figure 3 shows the whole process of this inquiry as a single flow diagram, while fig. 4 shows the proposed BLMS-ANNs paradigm. Using *nftool*, we examine six different RJF-HAP model variants and BLMS-ANN offer the answer.

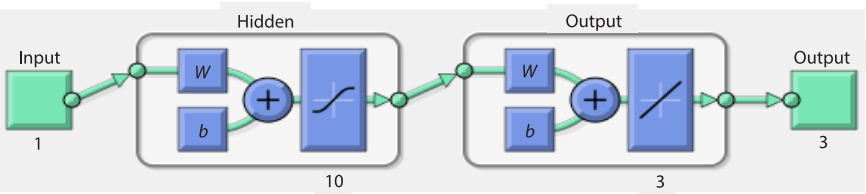

Figure 2. The architecture of neural network of the RJF-HAP model

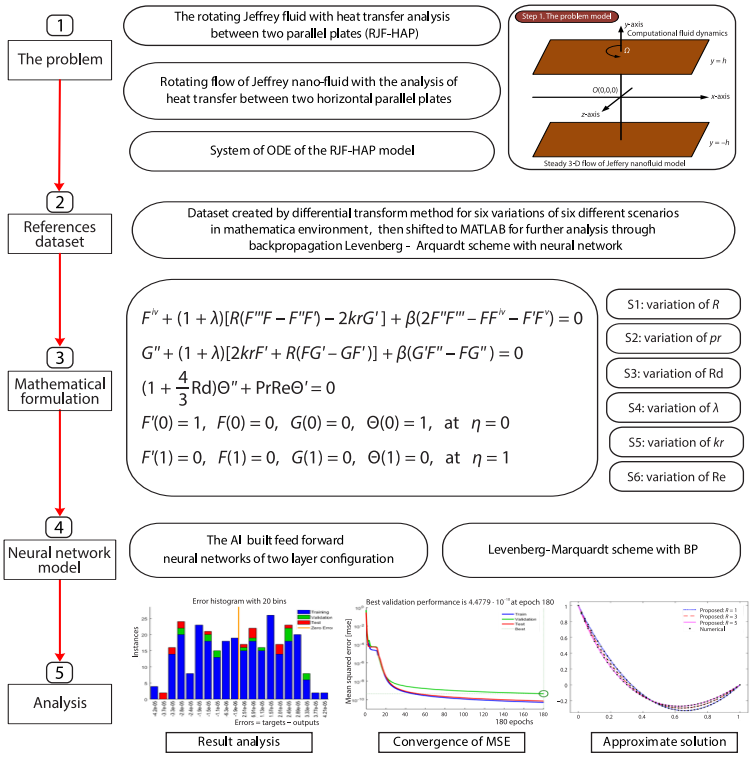

Figure 3. For the RJF-HAP model used the BLMS-ANN workflow method

For Cases 1-6. Figures 5-8 show the BLMS-ANN impacts on the RJF-HAP model. Both the first and second figures in the set display the six different cases MSE performance, fitting, and error histograms.

For Case 1. The R, Prandtl number, Rd, λ, kr, and Reynold number. For all four RJF-HAP scenarios, the regression analysis and state transitions are shown in figs. 6(a) and 6(b).

In the meantime, for Scenarios 1-6 of Case 1 in the RJF-HAP model. Table 1 lists the physically significant quantities.

For testing processes, sub figs. 5(i, ii) (a, b, c) determine the convergence of confirmation, training, and MSE evolutions for Scenarios 1-6 of RJF-HAP model. The performance is adept with MSE nearby $0.119\cdot10^{-9}$, $0694\cdot10^{-10}$, $0.795\cdot10^{-9}$, $0.634\cdot10^{-10}$, $0.595\cdot10^{-10}$, and $0.503\cdot10^{-10}$. The suggested method works better and more accurately when the MSE is less. Figures 5(i) and 5(ii) show the results of six different scenarios with inputs ranging from 0 to 1, a step size of 0.01 and the RJF-HAP model's

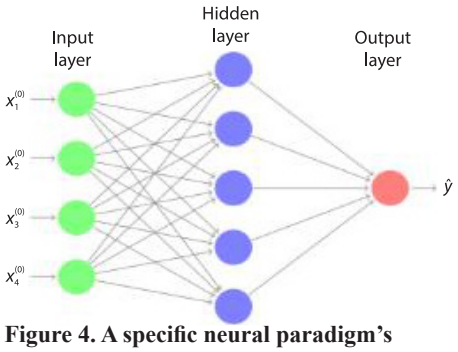

Figure 4. A specific neural paradigm's arrangement

Table 1. Potential use cases for the RJF-HAP model are explored across various scenarios

Scenario	Case	Physically significant quantities of notable interest						
		R	Pr	Rd	λ	kr	Re	β
1	1	1	1	0.4	3	0.1	3	0.1
	2	3	1	0.4	3	0.1	3	0.1
	3	5	1	0.4	3	0.1	3	0.1
2	1	1	0.7	0.4	3	0.1	3	0.1
	2	1	0.9	0.4	3	0.1	3	0.1
	3	1	1.1	0.4	3	0.1	3	0.1
3	1	1	1	0.3	3	0.1	3	0.1
	2	1	1	0.7	3	0.1	3	0.1
	3	1	1	0.8	3	0.1	3	0.1
4	1	1	1	0.4	1	0.1	3	0.1
	2	1	1	0.4	3	0.1	3	0.1
	3	1	1	0.4	5	0.1	3	0.1
5	1	5	1	0.4	3	0.1	3	0.1
	2	5	1	0.4	3	0.11	3	0.1
	3	5	1	0.4	3	0.12	3	0.1
6	1	1	1	0.4	3	0.1	1	0.1
	2	1	1	0.4	3	0.1	3	0.1
	3	1	1	0.4	3	0.1	5	0.1

efficiency. Using the numerical and associated conclusions from the Differential Transform method, we can verify the obtained outcomes and the plot of error dynamics. It is worth noting that the highest error for train, validation, and test is less than $1.74\cdot10^{-10}$, $0.160\cdot10^{-9}$, $0.195\cdot10^{-08}$, $0.114\cdot10^{-9}$, $0.147\cdot10^{-9}$, and $0.141\cdot10^{-9}$. The dynamics error and outputs of the RJF-HAP model for Case 1 of various situations for all inputs are also analyzed. This is in addition the error histograms that are displayed in figs. 5(i) and 5(ii). A comparison of the average value of the error bin with the zero line reveals an error that is close to $-1.9\cdot10^{-06}$, $-1.3\cdot10^{-06}$, $-1.6\cdot10^{-07}$, $-9.32\cdot10^{-07}$, and $-1.9\cdot10^{-06}$. The values of the gradient of Levenberg-Marquardt and the step size of Mu are quite near to each other, with the values being $1.00\cdot10^{-08}$, $1.00\cdot10^{-09}$, $1.00\cdot10^{-09}$, $1.00\cdot10^{-09}$, $1.00\cdot10^{-09}$, and $1.00\cdot10^{-09}$, along with $9.99\cdot10^{-08}$, $9.99\cdot10^{-08}$, $9.99\cdot10^{-08}$, $9.99\cdot10^{-08}$, $9.99\cdot10^{-08}$, and $9.99\cdot10^{-08}$ are presented in sub figs. 6(i) and 6(ii) (a, b, c).

Table 2. The consequences of BLMS-ANNS for Case 1-3

Scenario	Case	MSE			Execution	Gradient	Mu	Epoch	Time
		Training	Validation	Testing					
1	1	$1.1902\cdot10^{-10}$	$1.7448\cdot10^{-10}$	$1.3373\cdot10^{-10}$	$1.19\cdot10^{-10}$	$9.99\cdot10^{-08}$	$1\cdot10^{-08}$	208	3
	2	$3.5067\cdot10^{-10}$	$1.9697\cdot10^{-09}$	$1.4942\cdot10^{-10}$	$3.51\cdot10^{-10}$	$9.95\cdot10^{-10}$	$1\cdot10^{-08}$	315	2
	3	$2.8995\cdot10^{-10}$	$1.6285\cdot10^{-10}$	$1.9539\cdot10^{-10}$	$2.89\cdot10^{-10}$	$9.97\cdot10^{-08}$	$1\cdot10^{-08}$	338	2
2	1	$6.9358\cdot10^{-11}$	$1.6022\cdot10^{-10}$	$6.1822\cdot10^{-11}$	$6.94\cdot10^{-11}$	$9.99\cdot10^{-08}$	$1\cdot10^{-08}$	512	1
	2	$2.1763\cdot10^{-10}$	$4.5756\cdot10^{-10}$	$1.9357\cdot10^{-11}$	$2.17\cdot10^{-11}$	$9.94\cdot10^{-08}$	$1\cdot10^{-09}$	210	2
	3	$3.0689\cdot10^{-10}$	$1.0945\cdot10^{-10}$	$3.6237\cdot10^{-11}$	$3.07\cdot10^{-10}$	$9.93\cdot10^{-08}$	$1\cdot10^{-09}$	256	1
3	1	$7.9456\cdot10^{-10}$	$5.8137\cdot10^{-10}$	$1.9543\cdot10^{-09}$	$7.95\cdot10^{-10}$	$9.93\cdot10^{-08}$	$1\cdot10^{-09}$	385	1
	2	$5.9741\cdot10^{-11}$	$6.4587\cdot10^{-11}$	$8.3458\cdot10^{-11}$	$5.97\cdot10^{-11}$	$9.93\cdot10^{-08}$	$1\cdot10^{-08}$	343	1
	3	$6.4245\cdot10^{-11}$	$1.4403\cdot10^{-10}$	$1.1095\cdot10^{-10}$	$6.42\cdot10^{-10}$	$9.98\cdot10^{-08}$	$1\cdot10^{-08}$	495	1

Table 3. The consequences of BLMS-ANNS for Case 4-6

Ssenario	Case	MSE			Execution	Gradient	Mu	Epoch	Time
		Training	Validation	Testing					
4	1	$6.3472\cdot10^{-11}$	$1.5442\cdot10^{-11}$	$1.4148\cdot10^{-10}$	$6.34\cdot10^{-11}$	$9.98\cdot10^{-08}$	$1\cdot10^{-09}$	171	1
	2	5.6428E–10	$4.3942\cdot10^{-10}$	$1.4740\cdot10^{-10}$	$5.64\cdot10^{-10}$	$9.96\cdot10^{-08}$	$1\cdot10^{-09}$	173	1
	3	$5.1241\cdot10^{-1}1$	$1.2014\cdot10^{-11}$	$2.9285\cdot10^{-11}$	$5.12\cdot10^{-11}$	$9.95\cdot10^{-08}$	$1\cdot10^{-09}$	175	2
5	1	$5.9489\cdot10^{-1}1$	$1.4175\cdot10^{-10}$	$9.0535\cdot10^{-11}$	$5.95\cdot10^{-1}1$	$9.92\cdot10^{-08}$	$1\cdot10^{-09}$	171	2
	2	$5.4757\cdot10^{-10}$	$2.9447\cdot10^{-10}$	$6.5145\cdot10^{-10}$	$5.45\cdot10^{-10}$	$9.93\cdot10^{-08}$	$1\cdot10^{-09}$	168	1
	3	$4.8397\cdot10^{-11}$	$1.9341\cdot10^{-10}$	$1.3388\cdot10^{-10}$	$4.84\cdot10^{-11}$	$9.92\cdot10^{-08}$	$1\cdot10^{-09}$	169	1
5	1	$5.0305\cdot10^{-11}$	$4.4779\cdot10^{-10}$	$7.0974\cdot10^{-11}$	$5.03\cdot10^{-11}$	$9.86\cdot10^{-08}$	$1\cdot10^{-09}$	180	2
	2	$5.6034\cdot10^{-1}1$	$8.8148\cdot10^{-11}$	$7.1823\cdot10^{-11}$	$5.60\cdot10^{-11}$	$9.88\cdot10^{-08}$	$1\cdot10^{-09}$	186	2
	3	$5.5431\cdot10^{-10}$	$9.7908\cdot10^{-10}$	$1.2144\cdot10^{-09}$	$5.54\cdot10^{-1}0$	$9.95\cdot10^{-08}$	$1\cdot10^{-08}$	204	1

Case 1 of the RJF-HAP model demonstrates the capability, reliability, and convergence of BLMS-ANN through its results and visual representations. One typical way to classify data in regression analysis is via a correlation analysis. Results from testing, training, and validation of individual models all point to R-values close to one, demonstrating that BLMS-ANN resolves the RJF-HAP model effectively. For Case 1 of the different RJF-HAP model Scenarios 1-6, the corresponding numerical values in tabs. 2 and 3 show that the MSE performance for the proposed BLMS-ANN is close to 10^{-11}. Tables 2 and 3 present numerical results demonstrating that BLMS-ANN successfully executes the RJF-HAP model.

Figure 7(i) displays the results of the BLMS-ANN for the radial and tangential velocities, $G(\hat{y})$, and $\Theta(\hat{y})$, while fig. 7(ii) displays the results for the other six scenarios of the RJF-HAP paradigm. The influence on $F'(\eta)$ and $\Theta(\eta)$ due to the variation of R, Prandtl number, and Rd for RJF-HAP model Scenarios 1-3 is labelled in sub fig. 7(i) (a, b, c). Figure 7(i) (a) shows the variant in viscosity parameter for $F'(\eta)$. It is seen that higher values of viscosity parameter,

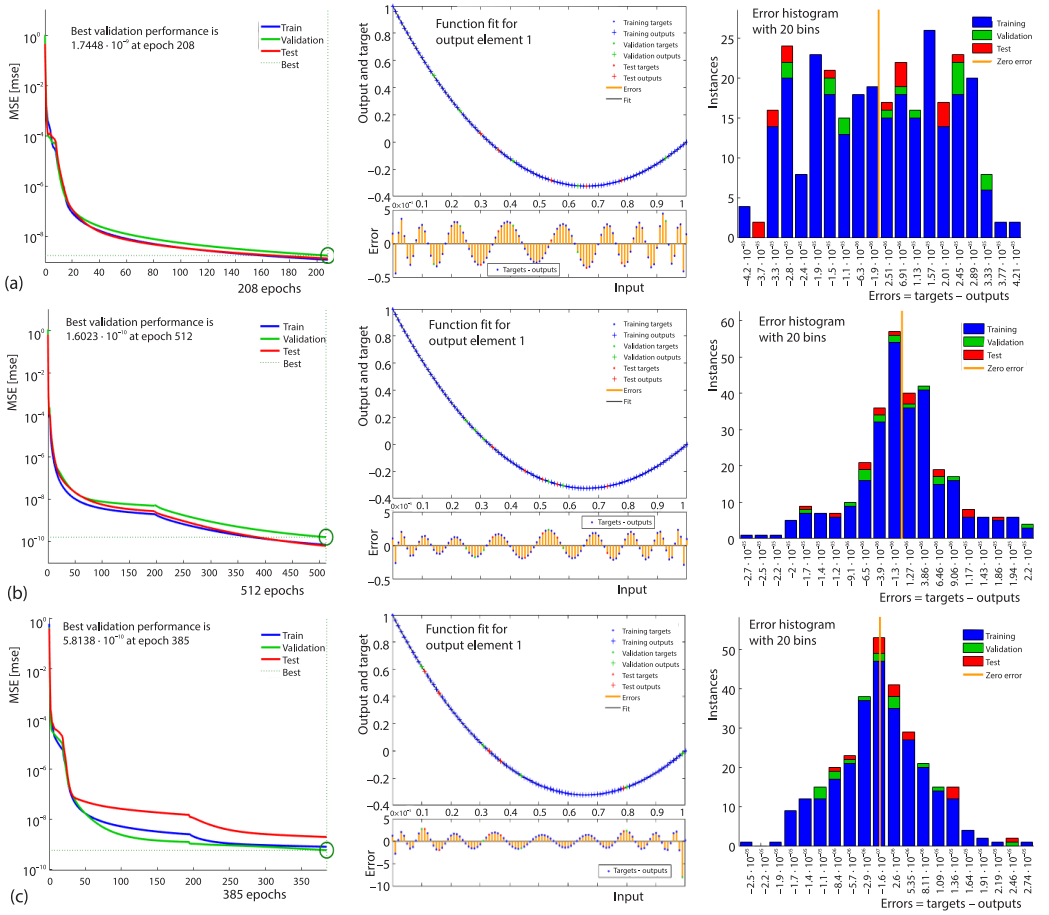

Figure 5(i). The MSE, fitness, and error histogram for Case-1 of Scenarios 1-3;
(a) MSE performance, fitness, and error fistogram for Case 1 of Scenario 1,
(b) MSE performance, fitness, and error histogram for Case 1 of Scenario 2, and
(c) MSE performance, fitness, and error histogram for Case 1 of Scenario 3

the velocity field retards and it happens due to the reason that viscosity of the fluid produces the resistance to the fluid-flow. Figure 7(i) (b) illustrates the influence of the Prandtl number on $\Theta(\eta)$. It is also observed that $\Theta(\eta)$ decreases as the Prandtl number increases, which is owing to larger levels of momentum diffusivity. Figure 7(i) (c) illustrates the influence of *Rd* on $\Theta(\eta)$. Radiation increases the heat created by the fluid's shear stresses, resulting in a rise in the fluid's temperature. As a result, for RJF-HAP model figs. 7(ii) (a, b, c) show the results of distinct magnitudes for Deborah number, λ, rotation parameter, *kr*, and Reynolds number for $F'(\eta)$, $G(\eta)$, and $\Theta(\eta)$ for Scenarios 4-6, respectively. Figure 7(ii) (a) describes the impact of Deborah number on the $F'(\eta)$. The velocity fields reduce with the increasing values of the Deborah number. Figure 7(ii) (b) depicts the effect of the rotation factor on $G(\eta)$ profile. It is obvious when the rotation parameter increases then it raises the fluid motion. Sub-fig. 7(ii) (c) shows the influence of the Reynolds number on $\Theta(\eta)$. The $\Theta(\eta)$ profile between two plates drops as Reynolds number upsurges.

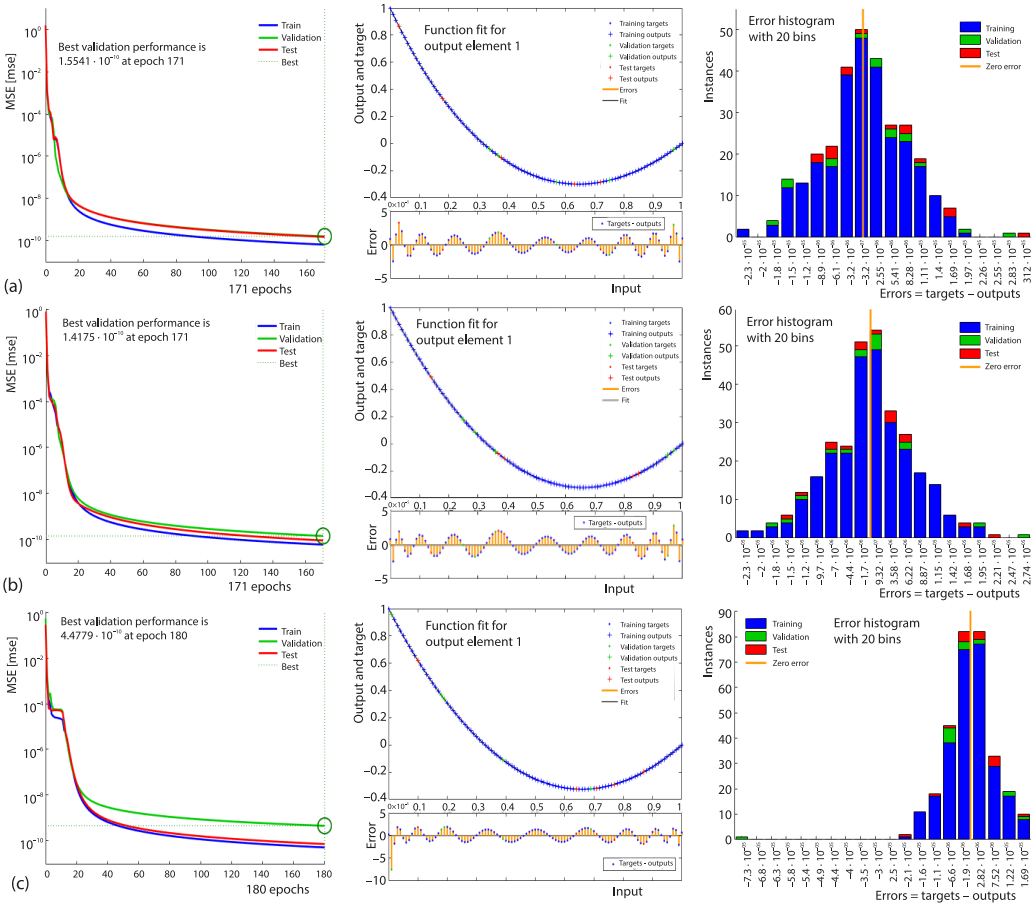

Figure 5(ii). The MSE performance, fitness, and error histogram for Case 1 of Scenarios 4-6; (a) MSE performance, fitness, and error histogram for Case 1 of Scenario 4, (b) MSE performance, fitness, and error histogram for Case 1 of Scenario 4, and (c) MSE performance, fitness, and error histogram for Case 1 of Scenario 6

As a result of the comparison between the results of BLMS-ANN and the conventional differential transform method solutions in Case 1 of all 6 scenarios, it was obtained that the absolute error was relatively match to the accurate measurements. This was demonstrated in sub-figs. 8(i) (a, b, c) and 8(ii) (a, b, c) for Scenarios 1-6.

In the sub fig. 8(i) (a, b, c), the absolute error accomplish values for Cases 1-3 for the $f'(\eta)$ and for $\theta(\eta)$ profile are 10^{-9} to 10^{-4}, 10^{-7} to 10^{-4}, and 10^{-7} to 10^{-4}, whereas for $f'(\eta)$ and for $\theta(\eta)$ profile in sub fig. 8(ii) (a, b, c), the error attain values for Cases 4-6, are 10^{-8} to 10^{-4}, 10^{-9} to 10^{-4}, and 10^{-7} to 10^{-4}, respectively.

Conclusions

This section includes the key features of the study. Here the RJF-HAP model is numerically studied to compute the Jeffrey nanofluid with heat transfer between two horizontal parallel plates.

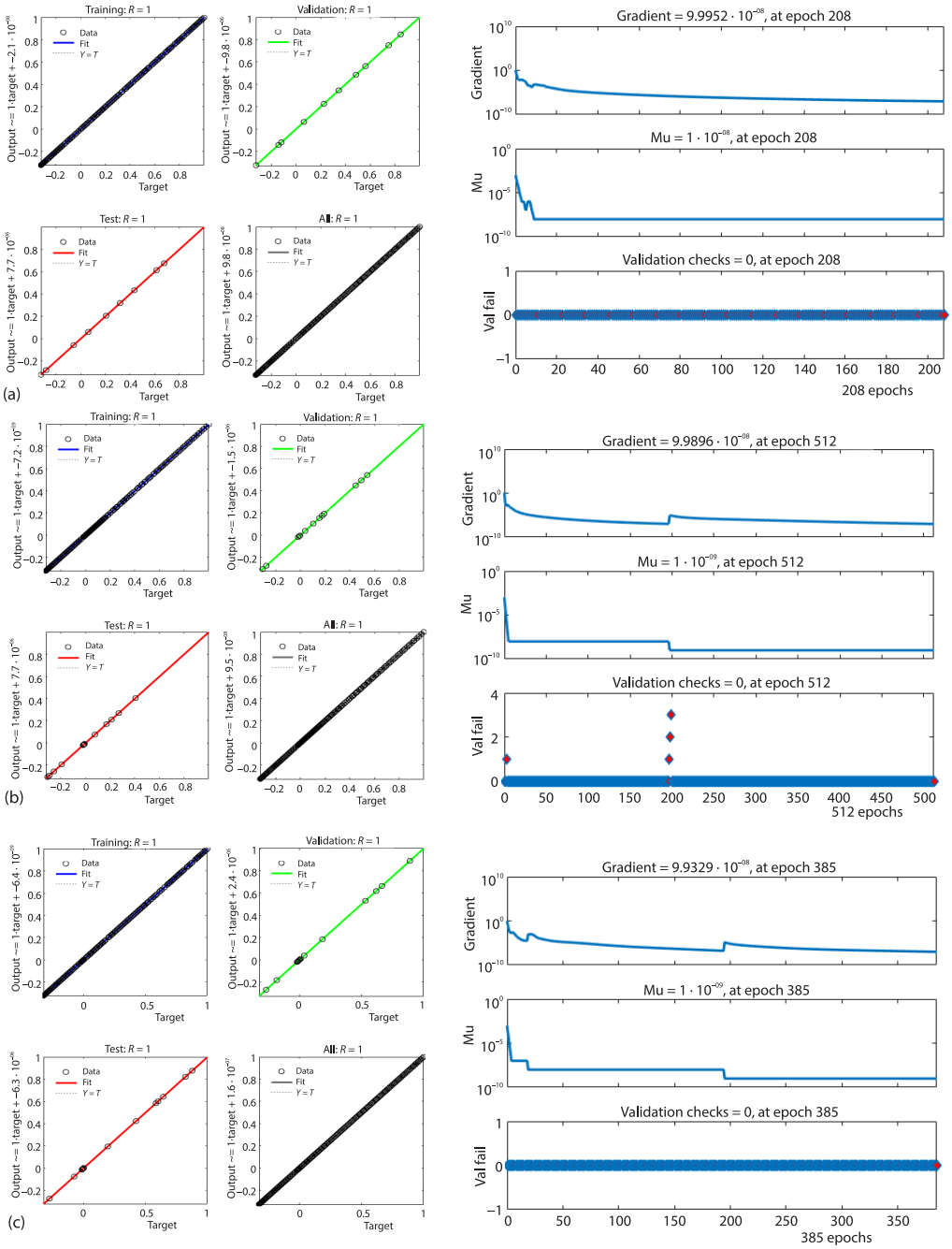

Figure 6(i). Regression analysis and state transition for Case 1 of Scenario 1-3;
(a) regression analysis and state transition for Case 1 of Scenario 1,
(b) regression analysis and state transition for Case 1 of Scenario 2, and
(c) regression analysis and state transition for Case 1 of Scenario 3

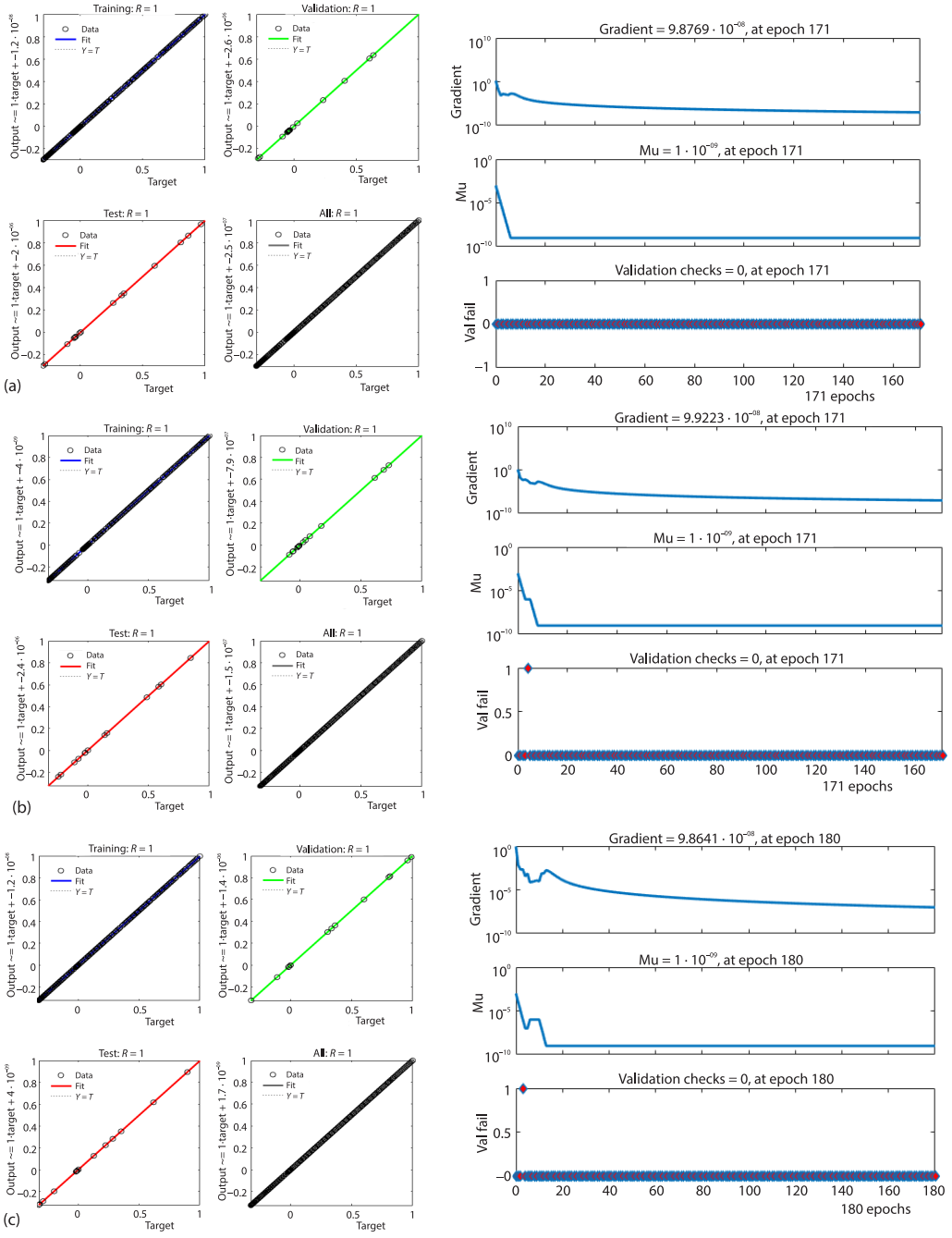

Figure 6(ii). Regression analysis and state transition for Case 1 of scenarios 4-6;
(a) regression analysis and state transition for Case 1 of Scenario 4,
(b) regression analysis and state transition for Case 1 of Scenario 5, and
(c) regression analysis and state transition for Case 1 of Scenario 6

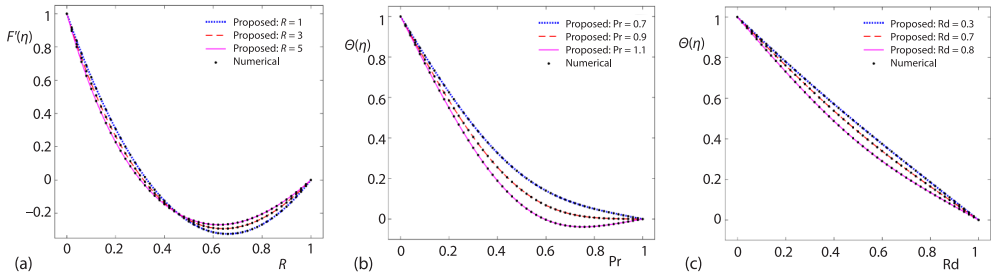

Figure 7(i). Analyzing the suggested BLMS-ANN and their numerical outcomes for the 1-3 RJF-HAP model scenarios; (a) impact of R on $F'(\eta)$, (b) impact of Prandtl number on $\theta(\eta)$, and (c) impact Rd of on $\Theta(\eta)$

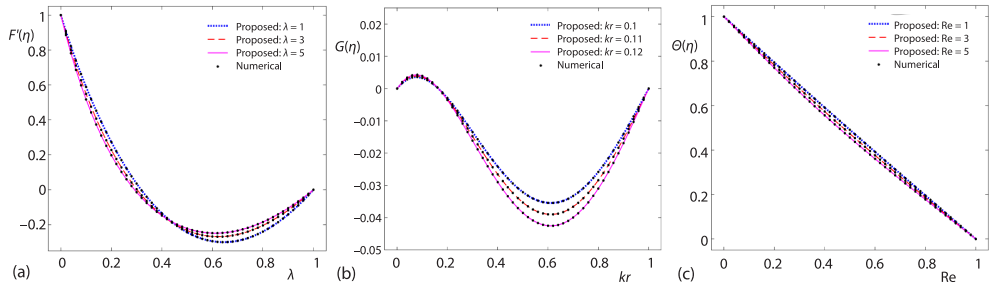

Figure 7(ii). Quantitative analysis of the suggested BLMS-ANN for the 4-6 RJF-HAP model scenarios; (a) impact of λ on $F'(\eta)$, (b) impact kr of on $G(\eta)$, and (c) impact of Reynolds number on $\Theta(\eta)$

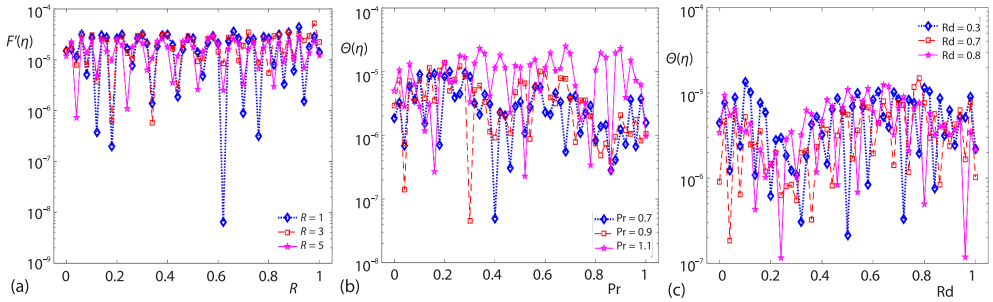

Figure 8(i). For the benchmark set of data, the results of the absolute error analysis are displayed, and the RJF-HAP model Scenarios 1-3 are analyzed with the help of the BLMS-ANN that are recommended; (a) absolute error of R on $F'(\eta)$, (b) absolute error of Prandtl number on $\Theta(\eta)$, and (c) absolute error of Rd on $\Theta(\eta)$

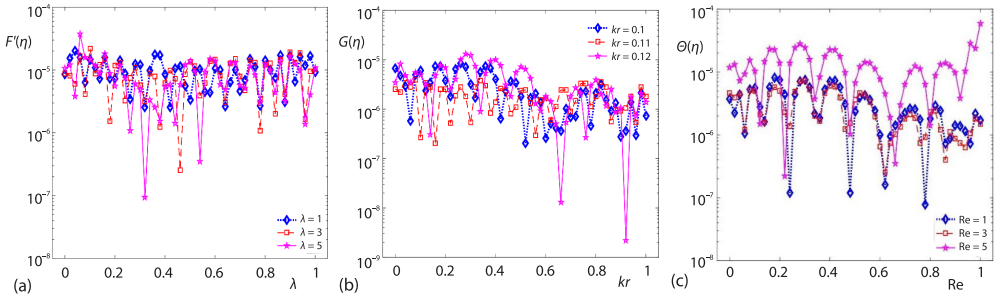

Figure 8(ii). For the benchmark set of data, the results of the absolute error analysis are displayed, and the RJF-HAP model Scenarios 4-6 are analyzed with the help of the BLMS-ANN that are recommended; (a) absolute error of λ on $F'(\eta)$, (b) absolute error of kr on $G(\eta)$, and (c) absolute error of Reynolds number on θ

- The process of constructing an ANN system that employs the LM technique with back BP is employed to investigate the solution of a present model that demonstrates the relationship between RJF-HAP and certain situations.
- Using proper correspondence variables, the PDE framework provides a description of the process of converting mathematical flow into a non-linear PDE framework.
- The RJF-HAP model relies on the data collected from the DTM, which contains variations from many physical parameters like the radiation parameter, Deborah number, viscosity parameter, Prandtl number, Reynolds number, and rotation parameter.
- The RJF-HAP reference dataset is constructed by varying different versions, with portions allocated for the validation, testing, and training 5%, 5%, and 90% of BLMS-ANN.
- The method's precision verifies a range of 10^{09} to 10^{11} for the suggested results, and this is corroborated by numerical and graphical depictions of convergence error histogram graphs, MSE, and regression dynamics.

References

[1] Schmidhuber, J., Deep Learning, *Scholarpedia*, *10* (2015), 11, pp. 85-117
[2] Werbos, P., *Applications of Advances in Non-Linear Sensitivity Analysis (PDF)*, System Modelling and Optimization, Springer, Heidelberg, Germany, 1982, pp. 762-770
[3] Ahmad, I., *et al*., Novel Applications of Intelligent Computing Paradigms for the Analysis of Non-Linear Reactive Transport Model of the Fluid in Soft Tissues and Microvessels, *Neural Computing and Applications*, *31* (2019), 12, pp. 9041-9059
[4] Shoaib, M., *et al*., Neuro-Computing Networks for Entropy Generation under the Influence of MHD and Thermal Radiation, *Surfaces and Interfaces*, *25* (2021), 101243
[5] Wang, L., *et al*, Investigating the Influence of the Wire-Arrays' Electrical Parameters on the Load Current of the z-Pinch Drivers, *AIP Advances*, *10* (2020), 6, 065024
[6] Uddin, I., *et al*., The Intelligent Networks for Double-Diffusion and MHD Analysis of Thin Film Flow over a Stretched Surface, *Scientific Reports*, *11* (2021), 1, pp. 1-20
[7] Ullah, H., *et al*., Neuro-Computing for Hall Current and MHD Effects on the Flow of Micro-Polar Nano-Fluid between Two Parallel Rotating Plates, *Arabian Journal for Science and Engineering*, 47 (2022), May, pp. 16371-16398
[8] Aljohani, J. L., *et al*., Supervised Learning Algorithm to Study the Magnetohydrodynamic Flow of a Third Grade Fluid for the Analysis of Wire Coating, *Arabian Journal for Science and Engineering*, *47* (2021), Sept., pp. 7505-7518
[9] Zokri, S. M., *et al*., The MHD Jeffrey Nanofluid Past a Stretching Sheet with Viscous Dissipationeffect, *J. Phys. Conf. Ser*., *890* (2017), 012002
[10] Hayat, T., *et al*., The 3-D Flow of a Jeffery Fluid over A Linearly Stretching Sheet, *Commun. Non-Linear Sci. Numer. Simul*., *17* (2012), 2, pp. 699-707
[11] Turkyilmazoglu, M. Pop, I. Exact Analytical Solutions for the Flow and Heat Transfer Near the Stagnation Point on a Stretching/Shrinking Sheet in a Jeffrey Fluid, *Int. J. Heat Mass Transfer*, *57* (2013), 1, pp. 82-88
[12] Shafique, Z., *et al.*, Boundary-Layer Flow of Maxwell Fluid Inrotating Frame with Binary Chemical Reaction and activation Energy, *Results Phys*., *6* (2016), C, pp. 627-633
[13] Nadeem, S., *et al*., Numerical Solution of non-Newtonian Nanofluid-flow Over a Stretching Sheet, *Appl. Nanosci*., *4* (2014), June, pp. 625-631
[14] Das, K., Influence of Slip and Heat Transfer on MHD Peristaltic Flow of a Jeffrey Fluid in an Inclined Asymmetric Porous Channel, *Indian Journal of Mathematics*, *54* (2012), 1, pp. 19-45
[15] Reddy, G. B., *et al*., Flow of a Jeffrey Fluid between Torsionally Oscillating Disks, *Ain Shams Engineering Journal*, 6 (2015), 1, pp. 355-362
[16] Shehzad, S. A., *et al.*, Non-Linear Thermal Radiation in 3-D Flow of Jeffrey Nanofluid: A Model for Solar Energy, *Applied Mathematics and Computation*, *248* (2014), Dec., pp. 273-286
[17] Hayat.T, *et al.*, The 3-D Rotating Flow of Jeffrey fluid for Cattaneo-Christov Heat Flux Model, *AIP Advances*, 6 (2016), 025012
[18] Kumari, A. B., *et al*., Effects of a Magnetic Field on the Free Convective Flow of Jeffrey Fluid Past an Infinite Vertical Porous Plate with Constant Heat Flux, *International Journal of Mathematical Archive*, 3 (2016), 6, pp. 2240-2248

[19] Farooq, A. A., *et al*., Lifting of a Jeffrey Fluid on a Vertical Belt under the Simultaneous Effects of Magnetic Field and Wall Slip Conditions, *International Journal of Advanced Mathematical*, *Sciences*, *1* (2013), 2, pp. 91-97
[20] Naveed, A., *et al*., The 2-D Flow of a Jeffrey Fluid in a Dilating and Squeezing Porous Channel, World Journal of Modelling and Simulation, *12* (2016), Dec., pp. 59-69
[21] Asadullah, M., *et al*., The MHD Flow of a Jeffrey Fluid in Converging and Diverging Channels, *International Journal of Modern Mathematical Sciences*, *6* (2013), 2, pp. 92-106
[22] Abbasi, F., Shehzad, S., Influence of Heat and Mass Flux Conditions in Hydromagnetic-Flow of Jeffrey Nanofluid, *AIP Advances*, *5* (2015), 3, 037111
[23] Khan, W. A., Pop, I., Boundary-Layer Flow of a Nanofluid Past a Stretching Sheet, *Int. J. Heat Mass Transfer*, *53* (2010), 11-12, pp. 2477-2483
[24] Eastman, J. A., *et al.*, Anomalously Increased Effective Thermal Conductivities of Ethylene Glycol-Based Nanofluids Containing Copper Nanoparticles, *Appl. Phys. Lett*., *78* (2001), 6, pp. 718-720
[25] Eastman, J. A., *et al*., Thermal Transport in Nanofluids, *Annu. Rev. Mater. Res*., *34* (2004), Aug., pp. 219-246
[26] Choi, S. U. S., Eastman, J. A., *Enhancing Thermal Conductivity of Fluids with Nanoparticles*, Tech. rep., Argonne National Lab., Lemont, Il., USA, 1995.
[27] Buongiorno, J., Convective Transport in Nanofluids, *J. Heat Transfer*, *128* (2006), 3, pp. 240-250
[28] Kuznetsov, A. V., Nield, D. A., Natural Convective Boundary-Layer Flow of a Nanofluid Past a Vertical Plate, *Int. J. Therm. Sci*., *49* (2010), 2, pp. 243-247
[29] Goyal, M., Bhargava, R., Numerical solution of MHD Viscoelastic Nanofluid-Flow over a Stretching Sheet with Partial Slip And Heat Source/Sink, in: *ISRN Nanotechnol*, Willy, New York, USA, 2013
[30] Turkyilmazoglu, M., Single Phase Nanofluids in Fluid Mechanics and Their Hydrodynamic Linear Stability Analysis, *Comput. Methods Programs Biomed*, *187* (2020), 105171
[31] Ahmed, F., *et al*., Numerical Simulation of Forced Convective Power Law Nanofluid through Circular Annulus Sector, *J. Therm. Anal. Calorim*., *135* (2019), May, pp. 861-871
[32] Karman, V., Uber, T., *Laminar and Turbulent Reibung*, *ZAMM*, (1921), pp. 233-235
[33] Greenspan, H.P., *The Theory of Rotating Fluids*, Cambridge University Press, Cambridge, UK, 1968, p. 327
[34] Vajravelua, K., Kumar B. V. R., Analytical and Numerical Solutions of a Coupled Non-Linear System Arising in a 3-D Rotating Flow, *International Journal of Non-Linear Mechanics*, *39* (2004), 1, pp. 13-24
[35] Turkyilmazoglu, M., The MHD Fluid-Flow and Heat Transfer Due to a Stretching Rotating Disk, *Int. J. Thermal Science*, *51* (2012), Jan., pp. 195-201
[36] Turkyilmazoglu. M.. Bödewadt Flow and Heat Transfer over a Stretching Stationary Disk, *Int. J. Mech Sci.*, *90* (2015), Jan., pp. 246-250
[37] Asghar. S., *et al*., Lie Group Analysis of Flow and Heat Transfer over a Stretching Rotating Disk, *Int. J. Heat Mass Transf*., *69* (2014), Feb., pp. 140-146
[38] Rashidi, M. M., *et al*., Parametric Analysis and Optimization of Entropy Generation in Unsteady MHD Flow over a Stretching Rotating Disk Using Artificial Neural Network and Particle Swarm Optimization Algorithm, *Energy*, *55* (2013), June, pp. 497-510
[39] Hayat, T., *et al*., Slip Flow by a Variable Thickness Rotating Disk Subject to Magneto-Hydrodynamics, *Results Phys*., *7* (2017), 5-6, pp. 503-509
[40] Bachok, N., *et al*., Flow and Heat Transfer over a Rotating Porous Disk in a Nanofluid, *Physica B*, *406* (2011), 9, pp. 1767-1772
[41] Hayat, T., *et al*., Radiative Flow Due to a Stretchable Rotating Disk with Variable Thickness, *Results Phys*., *7* (2017), 5, pp. 156-165
[42] Liao, S., On the Homotopy Analysis Method for Non-Linear Problems, *Applied Mathematics and Computation*, *147* (2004), 2, pp. 499-513
[43] Motsa, S. S., *et al*., Spectral Relaxation Method and Spectral Quasilinearization Method for Solving Unsteady Boundary-Layer Flow Problems, in: *Advances in Mathematical Physics*, Willy, New York, USA, 2014
[44] Wang, J., Ye, X., A Weak Galerkin Finite Element Method for Second-Order Elliptic Problems, *Journal of Computational and Applied Mathematics*, *241* (2013), Mar., pp. 103-115
[45] Sarif, N. M., *et al*., Numerical Solution of Flow and Heat Transfer over a Stretching Sheet with Newtonian Heating Using the Keller Box Method, *Procedia Engineering*, *53* (2013), 4, pp. 542-554
[46] Cheema, T. N., *et al*., Intelligent Computing with Levenberg-Marquardt Artificial Neural Networks for Non-Linear System of COVID-19 Epidemic Model for Future Generation Disease Control, *The European Physical Journal Plus*, *135* (2020), 11, pp. 1-35

[47] Umar, M., *et al*., A Stochastic Intelligent Computing with Neuro-Evolution Heuristics for Non-Linear SITR System of Novel COVID-19 Dynamics, *Symmetry*, *12* (2020), 10, 1628
[48] Bilal, H., *et al*., A Levenberg-Marquardt Backpropagation Method for Unsteady Squeezing Flow of Heat and Mass Transfer Behaviour between Parallel Plates, *Advances in Mechanical Engineering*, *13* (2021), 10, 16878140211040897
[49] Shoaib, M., *et al.*, Heat Transfer Impacts on Maxwell Nanofluid-Flow Over a Vertical Moving Surface with MHD Using Stochastic Numerical Technique Via Artificial Neural Networks, *Coatings*, *11* (2021), 12, 1483
[50] Akbar, A., *et al*., Intelligent Computing Paradigm For the Buongiorno Model of Nanofluid-Flow with Partial Slip and MHD Effects over a Rotating Disk, *ZAMM*, *103* (2023), 1, e202200141
[51] Khan, I., *et al*., Falkner-Skan Equation With Heat Transfer: A New Stochastic Numerical Approach, in: *Mathematical Problems in Engineering*, Willy, New York, USA, 2021, 1, 3921481
[52] Ullah, H., *et al.*, Numerical Treatment of Squeezed MHD Jeffrey Fluid-Flow with Cattaneo Chrisstov Heat Flux in a Rotating Frame Using Levnberg-Marquard Method, *Alexandria Engineering Journal*, *66* (2023), Mar., pp. 1031-1050
[53] Khan, I., *et al*., Design of Neural Network with Levenberg-Marquardt and Bayesian Regularization Backpropagation for Solving Pantograph Delay Differential Equations, *IEEE Access*, *8* (2020), 8, pp. 137918-137933
[54] Abbas, *et al*., Numerical simulation of Darcy-Forchheimer Flow of Casson Ternary Hybrid Nanofluid with Melting Phenomena and Local Thermal Non-Equilibrium Effects, *Case Studies in Thermal Engineering*, 60 (2024), 104694
[55] Ullah, H., *et al*., Thermal Radiation Effects of Ternary Hybrid Nanofluid-Flow in the Activation Energy: Numerical Computational Approach, *Results in Engineering*, *25* (2025), 104062
[56] Jose, J., Hotta, T. K., Thermal Performance Optimization of NanoEnhanced Phase Change Material-Based Heat Pipe Using Combined Artificial Neural Network and Genetic Algorithm Approach, *J. Thermal Sci. Eng. Appl. February*, *17* (2025), 2, 021002
[57] Shao, B., *et al.*, Numerical Study on the Effect of Various Working Fluids on the Performance of Loop Heat Pipes Based on 2-D Simulation, *J. Thermal Sci. Eng. Appl*., *17* (2025), 3, 031008
[58] Shubham, J. S., *et al.*, Numerical Analysis of Enhanced Forced Convection in Perforated Surface Wavy Plate-Fin Cores, *J. Thermal Sci. Eng. Appl*., *17* (2025), 5, 051004

Paper submitted: February 10, 2025
Paper revised: May 19, 2025
Paper accepted: July 21, 2025